Supplementary Information

First-principles evaluation of dopant impact on structural deformability and processability of $Li_7La_3Zr_2O_{12}$

A. Dive, K. Kim, S. Kang, L. F. Wan and B. Wood

Laboratory for Energy Applications for the Future (LEAF), Materials Science Division, Lawrence Livermore National Laboratory, Livermore, California 94551- 0808

Survey of the configurational space for doped LLZO

The unit cell of stoichiometric LLZO ($Li_7La_3Zr_2O_{12}$) comprises of 56 Li^+, 24 La^{3+} and 16 Zr^{4+} ions. In this study we consider three distinct dopants, i.e., Al^{3+} at Li^+ site, Ba^{2+} at La^{3+} site and Ta^{5+} at Zr^{4+} site and evaluate their impact on the deformability/sinterability of LLZO. Given the large number of available sites that the dopants can occupy, performing DFT relaxations for all possible configurations is not feasible. Instead, we devised certain thumb rules to down select configurations with the aim to correctly identify the ground state structure for different doping concentrations.

(a) Al-doped LLZO:
We have investigated Al^{3+} doping at Li^+ sites in $Li_7La_3Zr_2O_{12}$ (LLZO) unitcell as shown in Figure 1 of the main manuscript. Since Al^{3+} being a trivalent ion that occupies the Li^+ site, we need to remove two Li^+ ions in the structure to maintain charge neutrality within the unitcell. Figure S1(a) shows a representative doped LLZO structure with Al^{3+} occupying a 24d Li^+ site in cubic LLZO. The easiest approach is to remove Li^+ ions in the vicinity of Al^{3+} ion which would lower the repulsive interactions between Al^{3+} and nearby Li^+. Figure S1(b) shows the radial distribution functions (rdf), g(r) between Al-Li and the integrated g(r) that corresponds to the coordination number. The green line in Figure S1(b) shows the cutoff ~ 4.75 Å selected as the maximum distance that Li^+ would be removed around Al^{+3}. The first peak at ~ 2.5 Å corresponds to the first coordination shell of Li around Al, and the peaks between 2.5 Å and 4.75 Å corresponds to the second and third coordination shells. Based on the rdf analysis, we defined three distinct categories for Li^+ removal: (a) **C1:** Both the Li^+ ions removed belong to second nearest neighbors, (b) **C2:** Both the Li^+ ions removed belong to first nearest neighbors and (c) **C3:** One Li^+ belongs to first nearest neighbor and other Li^+ belongs to second nearest neighbors. We generated more 50 distinct structures based on above criteria for Li removal. Figure S1(c) shows the average total energy post relaxation for the three distinct categories suggesting that the Li^+ removal under category C3 to have lowest energy. As the number of possible neighboring Li^+ ions increase for distinct categories from C1 – C3, we observe marginal increase in the associated error bars. The variation in the average energy arises from the spacing between the generated vacancies. Closely spaced vacancies lead to increased energy corresponding to the upper limit for the average energy, whereas uniformly spaced vacancies generated by Li^+ removal leads to lower energy structures. The

energies in Figure S1(c) are for single Al substitution at the Li-site. Following this criterion of Li^+ ions removal and ensuring no inherent Al segregation, we generated series of structures for Al doping at 24d and 96h sites for smallest doping concentration ($Al_{0.25}Li_{6.25}La_3Zr_2O_{12}$). Figure S1(d) compares the energies for Al-doped LLZO at 24d and 96h sites. Al-doping at 24d sites show lower energies than Al-doping at 96h sites thereby suggesting preference of Al-doping at 24d sites in LLZO. As the number of available 96h sites are much greater than the available 24d sites for doping, we observe a larger variation in the average energy for Al-doping at 96h sites when compared to Al-doping at 24d sites.

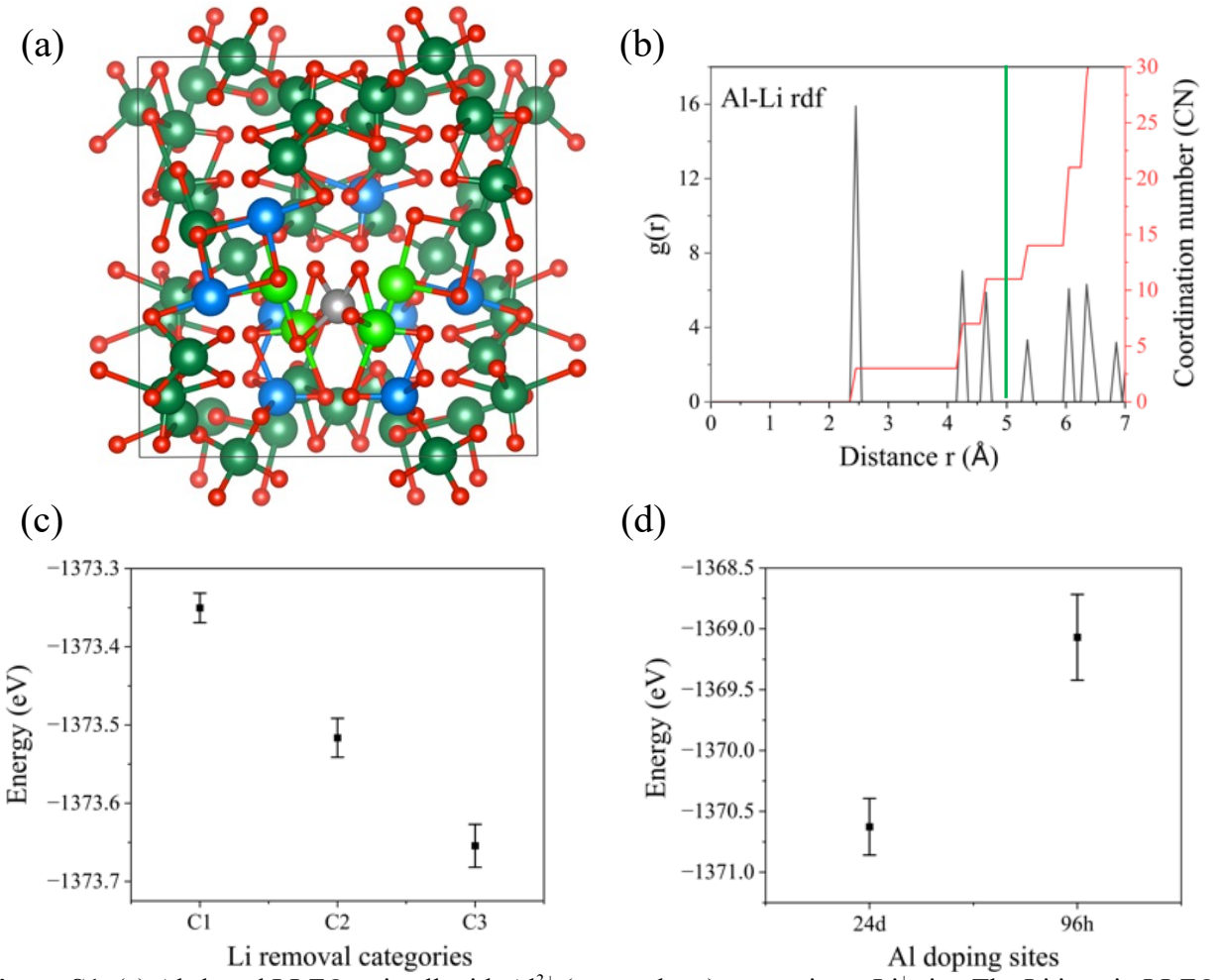

Figure S1. (a) Al-doped LLZO unitcell with Al^{3+} (grey sphere) occupying a Li^+ site. The Li ions in LLZO are represented by dark green spheres. The nearest Li^+ ions to Al are represented as light green spheres, whereas the Li^+ ions that are second nearest neighbors are represented as blue spheres. The red spheres represent the oxygen ions. The La and Zr ions are hidden to allow for easy visualization of the nearest and second nearest Li^+ ions around Al. (b) the rdf for Al-Li along with the respective coordination numbers is shown, (c) Show the average calculated total energies for Li removal for three distinct categories C1, C2 and C3 as defined earlier, (d) The average calculated total energies for Al^{3+} doping at two distinct Li^+ sites in LLZO are presented.

(b) Ba-doped LLZO:

We have investigated Ba^{2+} doping at La^{3+} sites in LLZO. Upon substitution of Ba^{2+} at a La^{3+} site, we need to add an additional Li^{+} in the unitcell to maintain charge neutrality. Figure S2 (b-d) shows the distinct open sites that Li^{+} can be inserted into. Figure S2(a) compares the average total energies post insertion Li^{+} ions at available open sites. The Li^{+} insertion at vacant 96h sites show lowest energies as compared to other available sites. As the number of available 96h sites is relatively greater than the 24d sites, we observe a relatively greater variation in the calculated average total energies represented by the error bars. Closely spaced Li^{+} ions insertion at 96h sites leads to high energy structures, whereas uniformly inserted Li^{+} ions yield low energy structures respectively. Consistent with these observations, we generated distinct Ba-doped LLZO structures with Li^{+} ions insertion following preference for 96h > 24d > 96h (close) respectively.

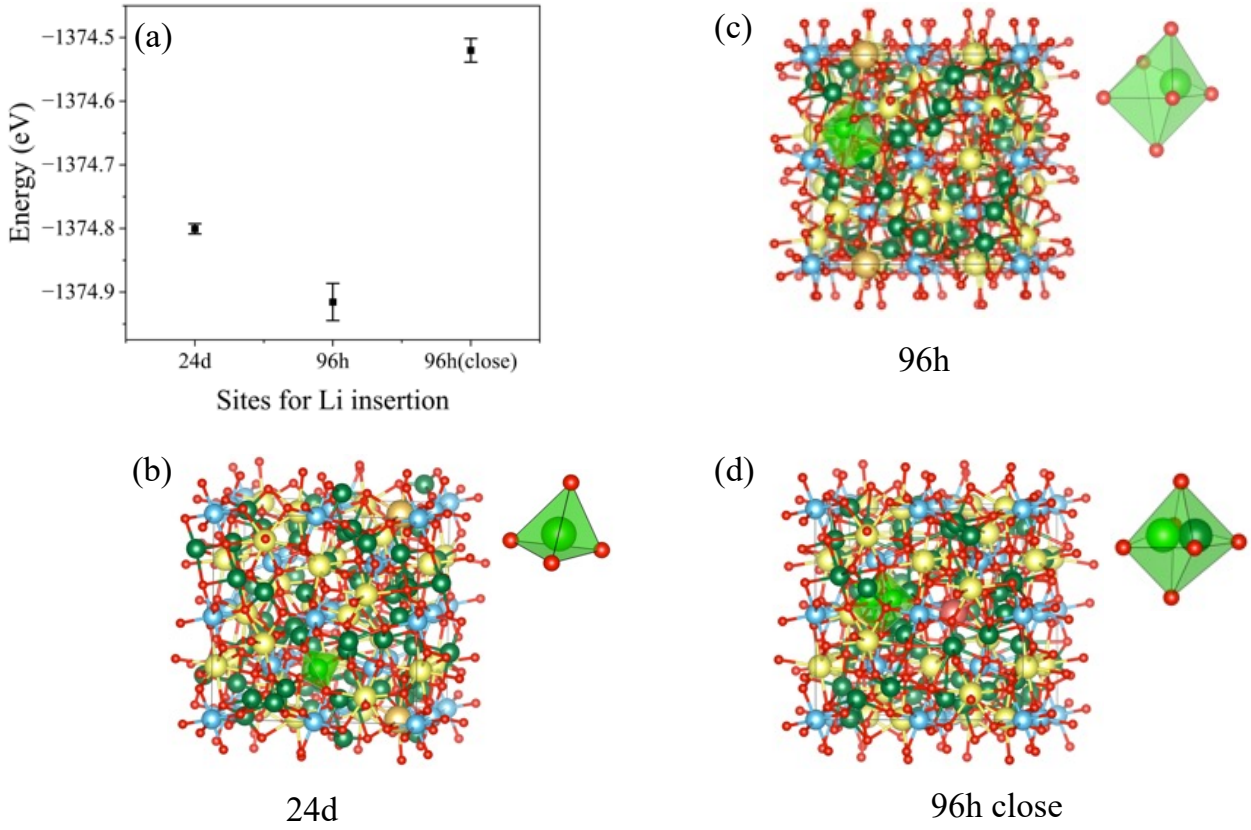

Figure S2. (a) The calculated average total energies for Li^{+} ions insertion at three distinct sites are shown. Three distinct sites namely (b) 24d, (c) 96h and (d) 96h close for Li^{+} insertion in Ba-doped LLZO unitcell are shown. Green, red, yellow, orange, and sky-blue spheres represent Li, O, La, Ba and Zr ions respectively. The light green spheres shown as zoomed out polyhedra represent the distinct sites at which the Li^{+} ions can be inserted.

(c) Ta-doped LLZO:

We have investigated Ta^{5+} doping at Zr^{4+} sites in LLZO. Substituting Ta^{5+} ion at Zr^{4+} site requires removal of one Li^{+} ion to maintain charge neutrality. Figure S3(a) shows a representative structure of LLZO with Ta^{5+} occupying a Zr^{4+} site. Figure S3(b) shows the rdf and coordination plot for Li^{+} ions around the Ta^{5+} ion in LLZO. Based on the rdf, we categorized Li removal distance from Ta into three groups: **D1:** Li ions within 3.0 Å from Ta (first peak in Figure S3(b)), **D2:** Li^{+} ions at a

distance above 3.0 Å and within 3.75 Å from Ta^{5+} (second peak in Figure S3(b)) and **D3:** Li^+ ions above 4.5 Å and within 5.3 Å from the Ta^{5+} ions (third and fourth small peaks in Figure S3(b)). The above categories distinguish Li^+ ions in three subsequent nearest neighbors based on the rdf shown in Figure S3(b). We generated a series of structures by removing Li^+ ions based on above categories and performed 0K relaxations for all generated structures. Figure S3(c) compares the energies of Ta^{5+} doped LLZO with Li^+ ion removed at distinct distance D1, D2, D3 as stated earlier. For the three distinct sites for Li^+ ions removal, we observe consistently large energy variations. As the number of available neighboring Li^+ ions (to be removed) is greater based on the rdf and CN plot in Figure S3 (b), we observe a relatively larger variation in the average total energies in Figure S3 (c). The variation is consistent throughout the distinct categories for Li^+ ions removal. Therefore, we observe that where exactly Li^+ ion is removed from the unit cell has negligible impact on the total energy of the resulting structure.

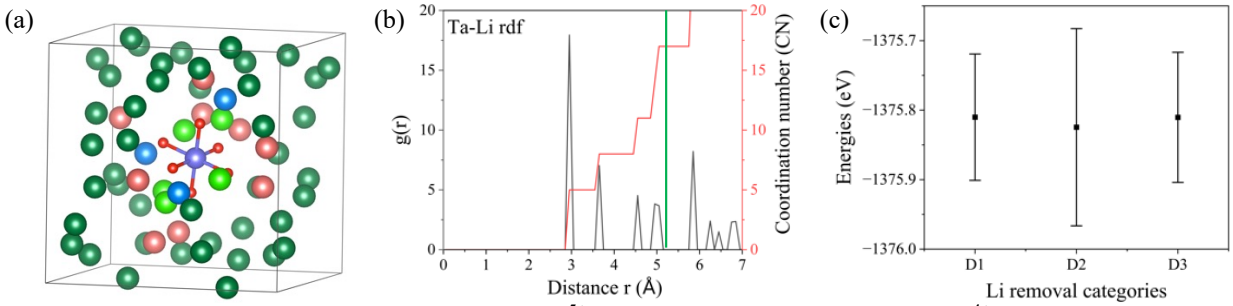

Figure S3. (a) Ta-doped LLZO unitcell with Ta^{5+} (purple sphere) occupying a Zr^{4+} site. The Li ions in LLZO are represented by dark green spheres. The nearest Li^+ ions to Ta are represented as light green spheres, whereas the Li^+ ions that are second nearest neighbors are represented as blue spheres. The pink spheres represent the Li+ ions contributing to the D3 category as stated earlier. The La, O and Zr ions are hidden to allow for easy visualization of the Li^+ ions around Ta. (b) the rdf for Ta-Li along with the respective coordination numbers is shown, (c) shows the average calculated energies for Li removal for three distinct categories D1, D2 and D3 as defined earlier.

Based on the above sensitivity analysis we established three key thumb rules for generating distinct structures of doped-LLZO:

1. For every Al^{3+} dopant occupying the Li^+ site in LLZO, one nearest and one second nearest Li^+ around Al^{3+} should be removed for the lowest energy configurations.
2. For Ba^{2+} dopant occupying the La^{3+} site in LLZO, Ba^{2+} prefers to be spaced far away (> 5.5 Å) with additional Li^+ ions to be added at the 96h vacant sites.
3. For Ta^{5+} dopant occupying Zr^{4+} site in LLZO, no preference of Li^+ ions removal around Ta^{5+} is observed.

Following these guidelines, we generated series of doped-LLZO configurations for each dopant and doping concentration. Figure S4 shows the distribution of energies for all configurations, from which we selected the lowest energy structure as the ground state for selected doped LLZO compositions.

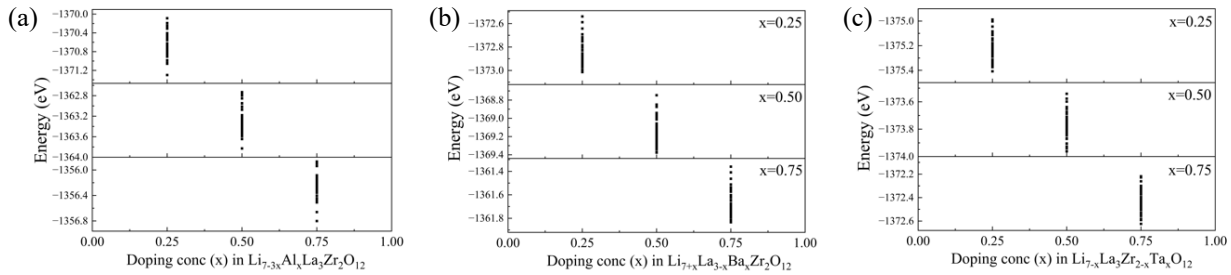

Figure S4. Energies for generated structures for (a) Al-doped LLZO, (b) Ba-doped LLZO and (c) Ta-doped LLZO at different doping concentrations are shown. The lowest energy structures from these are selected to be ground-state structures in the present study.

Calculations of elastic moduli

The bulk (B) and shear (G) moduli of undoped as well as doped LLZO were calculated by the Voigt-Reuss-Hill averaging scheme using the elastic tensor C_{ij} and the compliance tensor s_{ij} as [1-3]

$$B_{\mathrm{V}} = [(C_{11} + C_{22} + C_{33}) + 2(C_{12} + C_{23} + C_{31})]/9,$$
$$G_{\mathrm{V}} = [(C_{11} + C_{22} + C_{33}) - (C_{12} + C_{23} + C_{31}) + 3(C_{44} + C_{55} + C_{66})]/15,$$
$$s_{ij} = C_{ij}^{-1},$$
$$B_{\mathrm{R}} = 1/[(s_{11} + s_{22} + s_{33}) + 2(s_{12} + s_{23} + s_{31})],$$
$$G_{\mathrm{R}} = 15/[4(s_{11} + s_{22} + s_{33}) - 4(s_{12} + s_{23} + s_{31}) + 3(C_{44} + C_{55} + C_{66})],$$
$$B = (B_{\mathrm{V}} + B_{\mathrm{R}})/2, \text{ and}$$
$$G = (G_{\mathrm{V}} + G_{\mathrm{R}})/2.$$

Note that $C_{11} = C_{22} = C_{33}$, $C_{12} = C_{23} = C_{31}$, and $C_{44} = C_{55} = C_{66}$ for cubic symmetry. For each dopant composition we calculated the bulk and shear moduli for three distinct low energy structures from the structures as shown in Figure S4.

Calculations of amorphization energy

The amorphous phase for undoped and doped LLZO systems were achieved using the melt-and-quench method in *ab initio* molecular dynamics (AIMD). The LLZO unit cell comprised of 8 formula units of $Li_7La_3Zr_2O_{12}$ was heated to 3500 K and 3000 K for undoped and doped LLZO compositions, respectively. The melted phase was allowed to equilibrate for more than 2 – 3 ps at these high temperatures. Subsequently the melted phase was quenched to 300 K at a quenching rate of 350 K/ps to obtain the amorphous phase. The amorphous phase was further equilibrated at 300 K for 5 – 10 ps. The timestep utilized was 0.5 fs during heating, quenching, equilibrating and production runs. The energy of the amorphous/disordered phase ($E_{\mathrm{disordered}}$) was calculated by averaging the total energy over the 5 – 10 ps at 300 K. The energy for the crystalline phase ($E_{\mathrm{crystaline}}$) is the static ground state energy of the corresponding composition at 0 K. The $E_{\mathrm{disordered}}$ and $E_{\mathrm{crystaline}}$ are expressed as per formula unit (f.u.).

Calculations of the Lindemann ratio

The mean square displacement (MSD) was calculated from the 60 ps of AIMD production run. We utilized TRAVIS [4,5] analyzer to calculate the MSD using the equation below:

$$MSD = \lim_{\tau \to \infty} \frac{\langle ||r_i(t) - r_i(\tau)||^2 \rangle}{\tau}, \quad \ldots \text{(S1)}$$

where $r_i(t)$ denotes the position of atom i at time t. τ denotes the time lag which has been utilized to improve the statistics for MSD calculations by shifting time frames every τ timesteps. Figures S5 – 8 show the calculated MSD for La and Zr ions in undoped and doped LLZO at 1200 K and 1500 K.

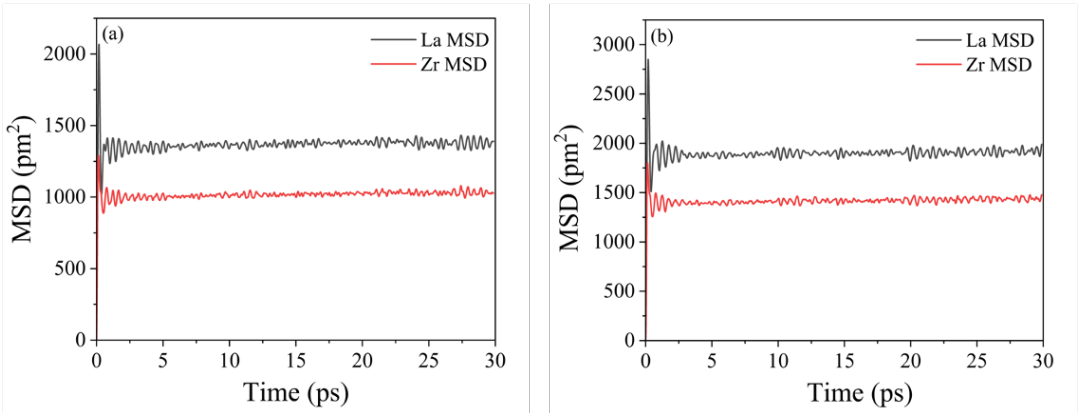

Figure S5. The calculated MSD over time for La and Zr ions in undoped LLZO at (a) 1200 K and (b) 1500 K from the AIMD trajectories.

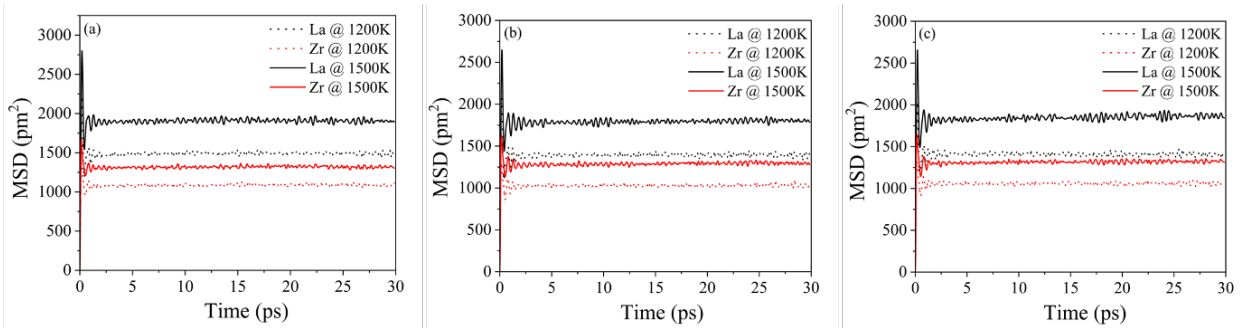

Figure S6. The calculated MSD over time for La and Zr ions in (a) $Al_{0.25}Li_{6.25}La_3Zr_2O_{12}$, (b) $Al_{0.50}Li_{5.5}La_3Zr_2O_{12}$ and (c) $Al_{0.75}Li_{4.75}La_3Zr_2O_{12}$ at 1200 K and 1500 K.

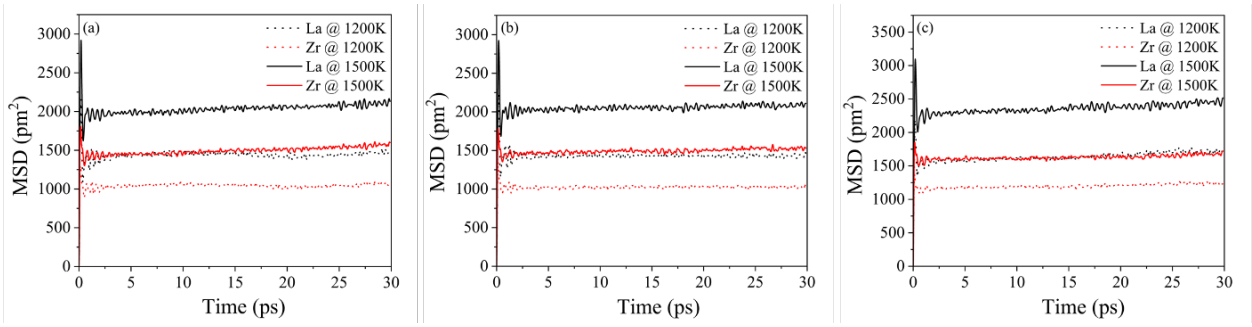

Figure S7. The calculated MSD over time for La and Zr ions in (a) $Li_{7.25}La_{2.75}Ba_{0.25}Zr_2O_{12}$, (b) $Li_{7.5}La_{2.5}Ba_{0.5}Zr_2O_{12}$and (c) $Li_{7.75}La_{2.25}Ba_{0.75}Zr_2O_{12}$ at 1200 K and 1500 K.

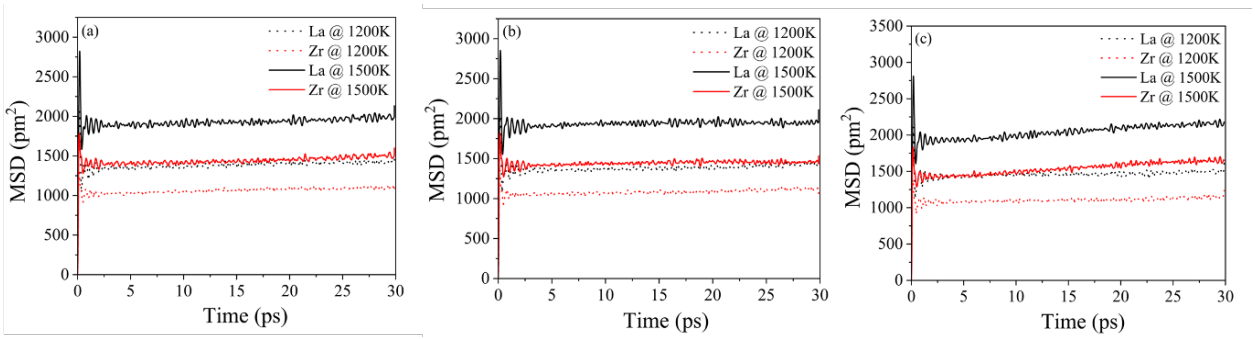

Figure S8. The calculated MSD over time for La and Zr ions in (a) $Li_{6.75}La_3Zr_{1.75}Ta_{0.25}O_{12}$, (b) $Li_{6.5}La_3Zr_{1.5}Ta_{0.5}O_{12}$ and (c) $Li_{6.25}La_3Zr_{1.25}Ta_{0.75}O_{12}$ at 1200 K and 1500 K.

Based on the MSD from these plots, we calculated the Lindemann ratio using the equation below:

$$Lindemann\ ratio = \frac{\sqrt{(MSD)}}{r_{\alpha\alpha}}, \quad \ldots (S2)$$

where $r_{\alpha\alpha}$ is the interatomic distance between La-La and Zr-Zr ion pairs determined from the radial distribution functions (RDFs) in Figure S9-12.

Calculations of radial distribution functions (RDFs)

The radial distribution function for species α and β as a function of distance *r*, $g_{\alpha\beta}(r)$, was calculated by

$$g_{\alpha\beta}(r) = \frac{1}{\rho_\beta N_\alpha} \langle \sum_j^{N_\alpha} \sum_{k \neq j}^{N_\beta} \delta(r - r_{jk}) \rangle \quad \ldots (S3)$$

where ρ_β is the number density of species β, N_α is the number of species α, and δ is the Dirac delta function with the distance r_{jk} between atom *j* of species α and atom *k* of species β.

Figures S9 – 12 show the RDF for La-La and Zr-Zr pairs for undoped and doped LLZO. The La-La and Zr-Zr distance for calculating the Lindemann ratio is determined from the edge of the first peak in the RDF plots. The value of $r_{\alpha\alpha}$ for La-La is averaged to 4.65 Å and 4.85 Å at 1200 K and 1500 K respectively. Similarly, the value of $r_{\alpha\alpha}$ for Zr-Zr is averaged to 6.12 Å and 6.25 Å at 1200 K and 1500 K.

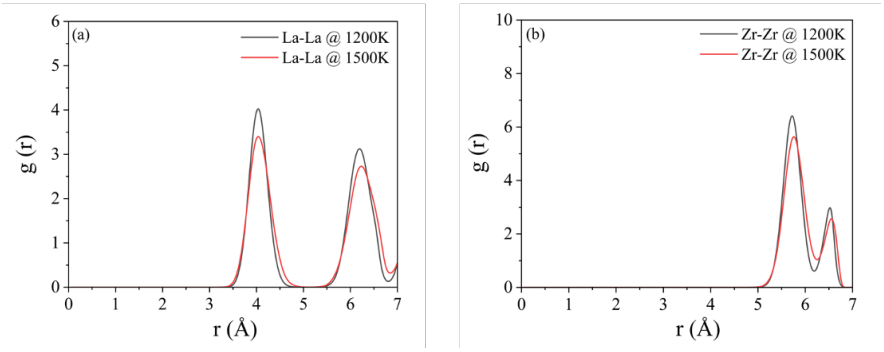

Figure S9. The RDF for (a) La-La and (b) Zr-Zr pairs for undoped LLZO at 1200K and 1500K.

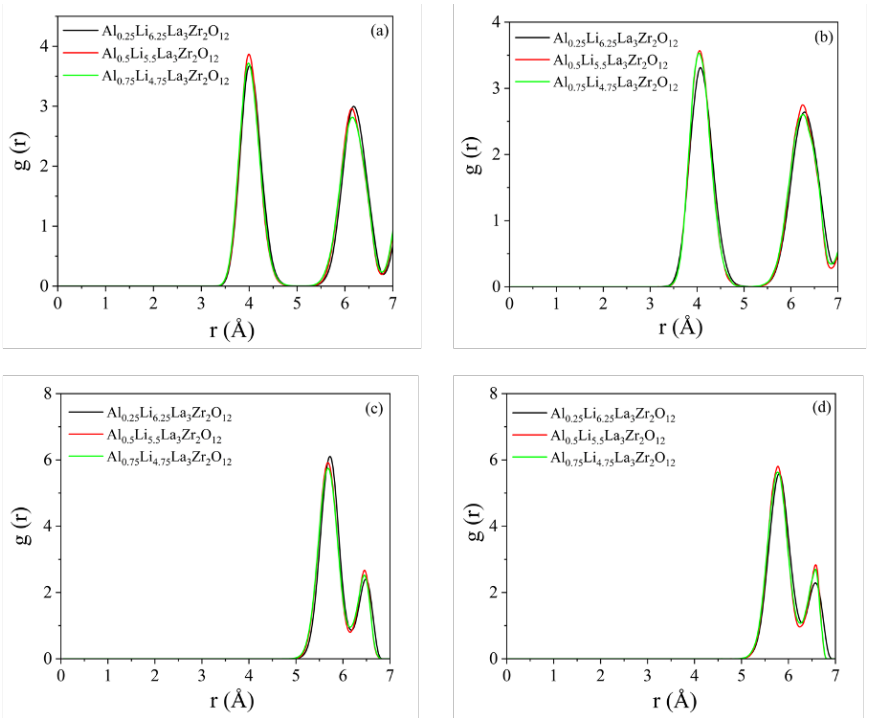

Figure S10. The RDFs for La-La pairs at (a) 1200 K and (b) 1500 K; and Zr-Zr pairs at (c) 1200 K and (d) 1500 K for Al-doped LLZO.

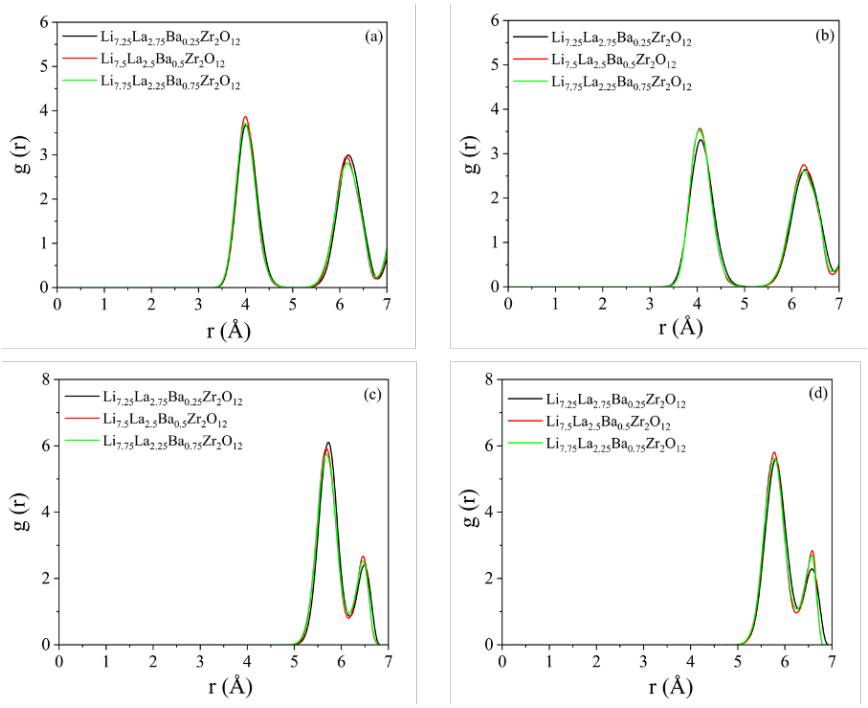

Figure S11. The RDFs for La-La pairs at (a) 1200 K and (b) 1500 K; and Zr-Zr pairs at (c) 1200 K and (d) 1500 K for Ba-doped LLZO.

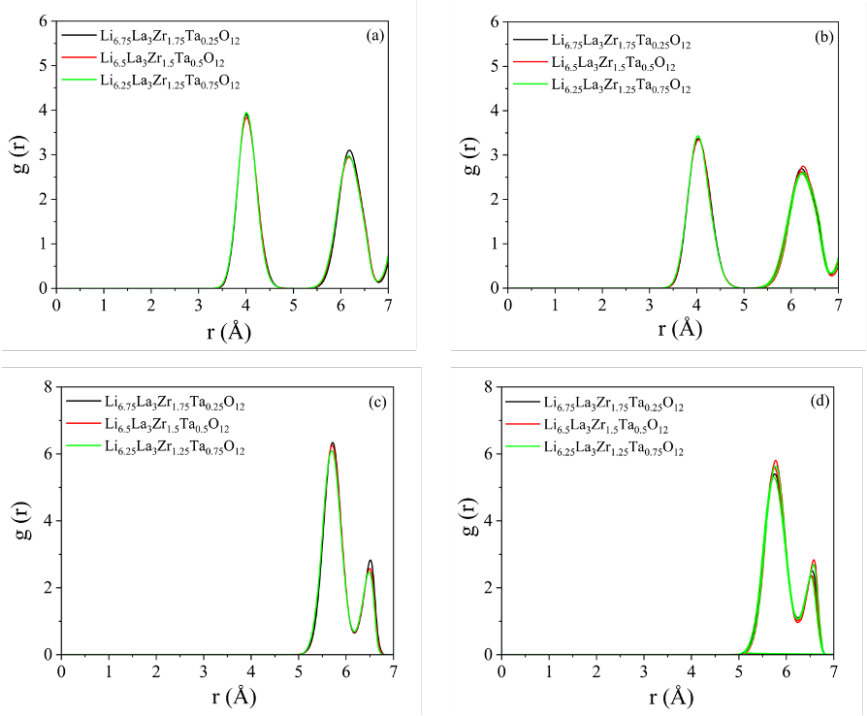

Figure S12. The RDFs for La-La pairs at (a) 1200 K and (b) 1500 K; and Zr-Zr pairs at (c) 1200 K and (d) 1500 K for Ta-doped LLZO.

Impact of dopants on the local bonding and structure:

Introducing dopants with distinct electronegativities at Li, La and Ta sites affects the nature of local bonding by changing the partial charges on the nearby oxygen atoms. Figure S13 shows the average partial charge (Bader charge) on O under different local environment wherein Al, Ba and Ta dopants are substituted for Li, La and Zr respectively. The average partial charge on oxygen shows a slight decrease in the partial charge by 0.05 e. This change in partial charge would introduce local distortions in the crystal structure by changing the nature of bonding between cation and oxygen. The extent of localized distortions can impact the different properties calculated in the manuscript. These effects are implicitly considered in DFT calculations, for which each doped LLZO structure were kept charge neutral. The extent of localized distortions is calculated utilizing the continuous shape measure (CSM) values as described in the next section.

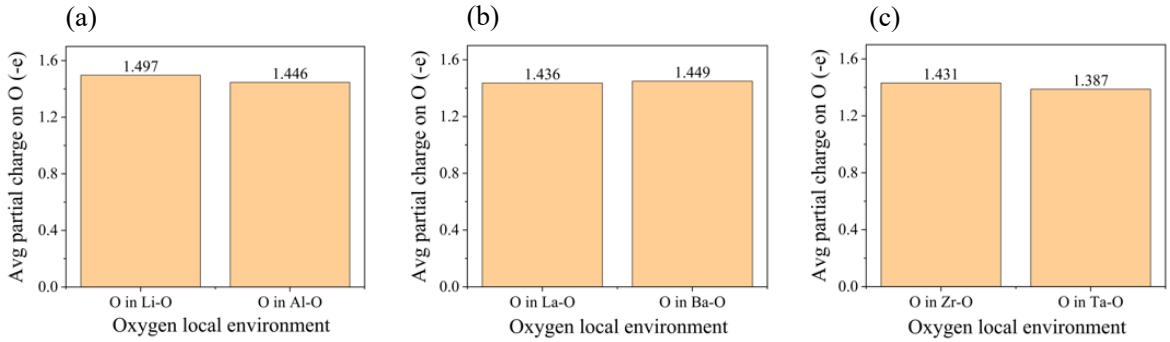

Figure S13. The average partial charge on oxygen ions in distinct local environment (a) Li/Al polyhedra, (b) La/Ba polyhedra and (c) Zr/Ta polyhedra are shown.

Calculations of the continuous shape measure (CSM)

The extent of distortion of the ZrO_6 and the LaO_8 polyhedra at 1200 K, 1500 K and 1800K were calculated using the SHAPE 2.1 package [6 – 8]. The SHAPE measures the degree of distortion of the polyhedra by calculating the continuous shape measure (CSM) based on Equation S5 below:

$$CSM = \frac{\sum_1^N |Q_k - P_k|^2}{\sum_1^N |Q_k - Q_0|^2} \times 100\%, \quad \ldots (S4)$$

where N is the number of vertices in the polyhedra (8 for LaO_8 and 6 for ZrO_6), Q_k is the coordinate vector for each vertex in the given polyhedra for which the CSM is being calculated, and P_k is the coordinate vector for each vertex of the nearest possible polyhedra with reference to the given polyhedra matching the reference symmetry of polyhedra. The reference symmetry of the polyhedra is considered from a cubic LLZO unit cell optimized at 0 K. Q_0 is the coordinate vector of the center of mass of the given polyhedra for which CSM is being calculated. The calculated CSM value provides the degree of deviation (CSM x 100 %) from the reference symmetry, and hence the CSM value of 0 corresponds to a perfectly matching symmetry of 0% deviation from the reference polyhedra. The CSM values were calculated for both LaO_8 and ZrO_6 polyhedra for the last 30 ps of AIMD trajectory from the production runs using an interval of 0.25 ps for each of the La and Zr ions. The CSM values were time-averaged for each ion, and then the mean and standard deviation for the time-averaged CSM values for all the ions were calculated. Figure S14 (a-d) shows the mean CSM for LaO_8 polyhedra in undoped and doped LLZO unit cell at 1200 K, 1500 K and 1800 K respectively. To understand the impact of temperature on the extent of distortion of the polyhedra, we plotted the mean CSM vs 1000/T as shown in Figure S14 (a-d) and S15 (a-d) for LaO_8 and ZrO_6 polyhedra respectively.

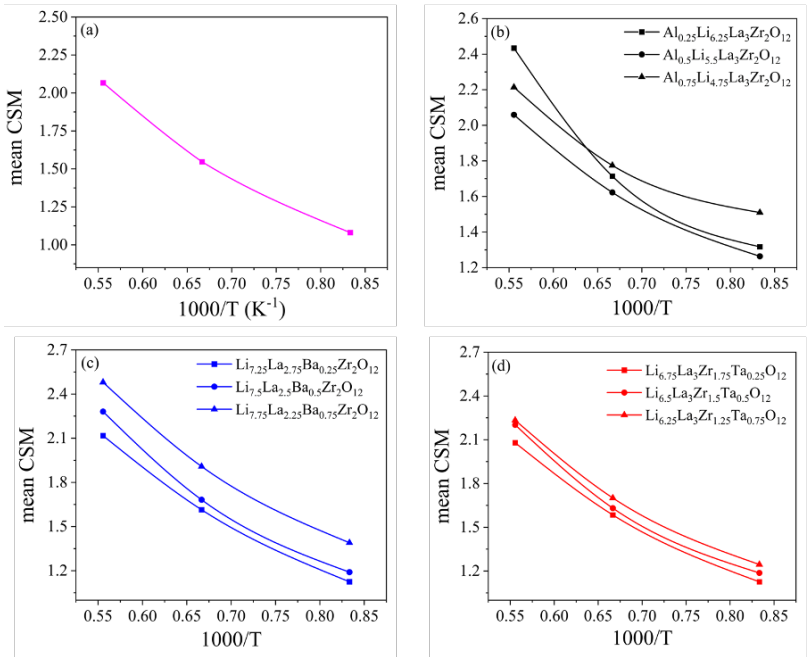

Figure S14. The mean CSM for LaO_8 polyhedra in (a) undoped, (b) Al-doped, (c) Ba-doped and (d) Ta-doped LLZO for three distinct temperatures is shown.

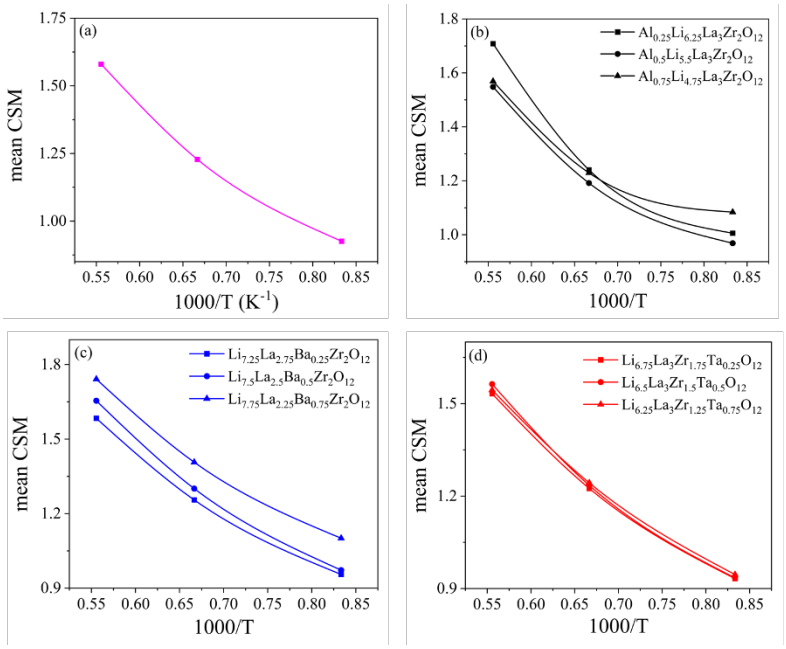

Figure S15. The mean CSM for ZrO_6 polyhedra in (a) undoped, (b) Al-doped, (c) Ba-doped and (d) Ta-doped LLZO for three distinct temperatures is shown.

The plots in Figure S14 and S15 show the mean CSM following an exponential behavior with temperature (T). Therefore, to evaluate the sensitivity of CSM values against temperature, we employ exponential fitting using the Equation S5 below to determine the E_{disT}:

$$CSM = C_0 \times e^{\left(\frac{-E_{disT}}{T}\right)}, \quad \ldots (S5)$$

where CSM is mean CSM calculated as stated above and T is the temperature in K. The logarithmic form of equation S5 would yield a linear relationship between log (mean CSM) and temperature (T) shown as inset in Figure 4 (c, d) in the main manuscript. E_{disT} provides an estimate of relative ease of inducing thermal distortions of polyhedral unit in the LLZO lattice.

Calculations of the surface energies and surface disordering energies

The surface models were constructed starting from symmetric $Li_{7.5}La_3Zr_2O_{12}$ slab model. The charge balance was achieved by removing atoms considering the site-energy of each element (see below), which results in $Li_7La_3Zr_2O_{12}$ stoichiometry. The surface-termination species (e.g., Li in (100) Li surface) was removed from the center area of the slab model (which mimics the bulk $Li_7La_3Zr_2O_{12}$ behavior) to make the termination species rich on the surface, whereas other species was removed from near-surface regions. At least 40% of the entire slab thickness is considered as the bulk area at the center of the model. We selected atoms to remove by comparing relative total energies between removal sites (without relaxation for a sake of reducing computation cost), except Li atoms. Our tests showed that the random removal of Li atoms results in 7.5 meV/atom difference at most. The doping of Al (at Li site), Ba (at La site), and Ta (at Zr site) was performed on the near-surface area to maximize the effect of doping on surface. The thickness of vacuum area was set to 12 Å, and each slab model has following sizes: 13.00 × 13.00 × 34.12 Å^3 with 312 atoms in (100) Li, 11.26 × 11.26 × 35.55 Å^3 (α = 70.53º) with 240 atoms in (110) Li and (110) La, 11.26 × 11.26 × 41.88 Å^3 (α = 70.53º) with 312 atoms in (110) O, 18.39 × 18.39 × 29.35 Å^3 (α = 120º) with 432 atoms in (111) Li, and 18.39 × 18.39 × 29.02 Å^3 (α = 120º) with 432 atoms in (111) Zr surfaces

(note that the number of atoms corresponds to models before doping). The surface energy (σ) was evaluated using equation S6 below:

$$\sigma = \frac{1}{2A}\left(E_{\text{Slab}} - n_{\text{f.u.}} \times E_{\text{bulk}}^{\text{LLZO}}\right) \quad \ldots \text{(S6)}$$

where A is the surface area, E_{Slab} is the total energy of the slab model, $n_{\text{f.u.}}$ is the number of formula unit (f.u.) in the slab, and $E_{\text{bulk}}^{\text{LLZO}}$ is the total energy bulk LLZO per f.u. For the surface energy calculations in Equation S6, it is difficult to obtain the total energy of doped LLZO bulk systems with the same stoichiometry of slab models (e.g., the Li stoichiometry in (100) Li slab model is 6.308). We found that the total energy of doped LLZO is linearly proportional to the doping concentration, thus we used the interpolation scheme to estimate the total energy of doped LLZO bulk systems.

The surface disordering energy was calculated using Equation S7, where $E_{\text{disordered}}$ and E_{ordered} were obtained using five snapshots collected every 0.5 ps at the end of AIMD simulations (simulation length longer than 5 ps with 1 fs time step) at temperatures with and without surface disorder. The total energies of five snapshots were averaged after ionic relaxation. The uncertainty of the surface disordering energy was determined by the standard deviation σ of the five energies as

$$\Delta E_{\text{SDE}} = \pm\frac{1}{2A}\{[(E_{\text{disordered}} + \sigma_{\text{disordered}}) - (E_{\text{ordered}} + \sigma_{\text{ordered}})] - E_{\text{SDE}}\} \quad \ldots \text{(S7)}$$

For the (100) Li surface models, the snapshots without surface disorder were collected at 1200 K and those with the disorder (but no disorder at the center area of the model) were sampled between 1400 and 1600 K. As complete melting occurs at different temperatures with different doping elements and levels, the temperatures to obtain ordered and disordered surface samples vary depending on systems. For the (111) Zr surface models, those temperatures were between 900 and 1000 K without surface disorder and between 1200 and 1300 K with the disorder.

Calculations of the Li^+ diffusivity and activation energy

The diffusivity D of Li^+ ion was calculated using the mean squared displacement as

$$D = \frac{1}{2d}\frac{\langle||r_i(t) - r_i(\tau)||^2\rangle}{\tau}, \quad \ldots \text{(S8)}$$

where $d = 3$ is the dimensionality of the system and r_i is the position of atom i. $\frac{\langle||r_i(t) - r_i(\tau)||^2\rangle}{\tau}$ is the mean squared displacement which is determined from the ab initio MD trajectories at three distinct temperatures 1200K, 1500K and 1800K respectively. Then, the activation energy E_a was estimated by fitting the diffusivity data at 1200 K, 1500 K and 1800 K to the Arrhenius relation as

$$D(T) = D_0 \exp[-E_a/k_B T] \quad \ldots \text{(S9)}$$

where D_0 is a prefactor, and k_B is the Boltzmann constant.

Calculations of the *Ease of Sintering*

The *Ease of Sintering* is calculated using Equation S10:

$$Ease\ of\ Sintering = \frac{P_{doped} - P_{undoped}}{\sigma_P}, \quad \ldots (S10)$$

where P_{doped} and $P_{undoped}$ are the calculated absolute values as reported in the Main manuscript (Figure 2-6) for doped and undoped LLZO respectively.

For the *External stress* descriptor, we considered bulk and shear moduli as those contributing equally towards the material response to external stress. We first calculated the standard deviation σ_P for bulk and shear moduli respectively, and then using the Equation S10, we determined the *Ease of Sintering* values for each bulk and shear moduli. The *Ease of Sintering* for *External stress* descriptors is calculated by taking average of the *Ease of Sintering* values for bulk and shear modulus.
The *Bond disorder* descriptor was calculated using the La and Zr Lindemann Ratio. We first calculated the *Ease of Sintering* for both La and Zr Lindemann Ratio individually using Equation S10 and then took the average value to finally determine the *Ease of Sintering* for the *Bond disorder* descriptor.
For the *Polyhedra disorder*, we first determined the *Ease of Sintering* for four properties which are the mean CSM and E_{disT} values for LaO_8 and ZrO_6 polyhedra using equation S10. Subsequently the *Ease of Sintering* for Polyhedra disorder descriptor was calculated by taking the average value of each of the above individual contributions.
The *Bulk disorder* descriptor considers the amorphization energy calculated for all the undoped and doped LLZO compositions. Therefore, the *Ease of Sintering* for *Bulk disorder* is *Ease of Sintering* calculations for amorphization energy using Equation S10.
Lastly, the *Surface Kinetics* descriptor values are obtained by averaging the *Ease of sintering* values of Li-term, La-term and Zr-term surface energies and surface disordering energies of (100) Li and (111) Zr surfaces.

References:

1. R. Hill, Proceedings of the Physical Society. Section A, 1952, **65**, 349-354.
2. A. Reuss, Z. Angew. Math. Mech., 1929, **9**, 49-58.
3. W. Voigt, Lehrbuch Der Kristallphysik, Taubner, Leipzig, 1928.
4. M. Brehm, M. Thomas, S. Gehrke, and B. Kirchner, J. Chem. Phys., 2020, 152, 164105.
5. M. Brehm and B. Kirchner, J. Chem. Inf. Model., 2011, 51(8), 2007–2023.
6. M. Pinsky, D. Avnir. Inorg. Chem., 1998, 37, 5575.
7. D. Casanova, J. Cirera, M. Llunell, P. Alemany, D. Avnir, S. Alvarez. J. Am. Chem. Soc., 2004, 126, 1755-1763.
8. J. Cirera, E. Ruiz, S. Alvarez. Chem. Eur. J., 2006, 12, 3162